Catal Lett
DOI 10.1007/s10562-015-1507-6

Enhanced CO and Soot Oxidation Activity Over Y-Doped Ceria–Zirconia and Ceria–Lanthana Solid Solutions

D. Devaiah · T. Tsuzuki · C. U. Aniz · B. M. Reddy

Received: 26 December 2014 / Accepted: 28 February 2015

Abstract Y-doped ceria–zirconia ($Ce_{0.8}Zr_{0.12}Y_{0.08}O_{2-\delta}$, CZY) and ceria–lanthana ($Ce_{0.8}La_{0.12}Y_{0.08}O_{2-\delta}$, CLY) ternary oxide solid solutions were synthesized by a facile coprecipitation method. Structural, textural, redox, and morphological properties of the synthesized samples were investigated by means of X-ray diffraction (XRD), inductively coupled plasma-optical emission spectroscopy (ICP–OES), Raman spectroscopy (RS), UV–visible diffuse reflectance spectroscopy (UV–vis DRS), X-ray photoelectron spectroscopy (XPS), temperature-programmed reduction by hydrogen (H_2-TPR), high resolution transmission electron microscopy (HRTEM), and Brunauer–Emmett–Teller surface area (BET SA) techniques. The formation of ternary oxide solid solutions was confirmed from XRD, RS, and UV–vis DRS results. ICP–OES analysis confirmed the elemental composition in the ternary oxide solid solutions. HRTEM images revealed irregular morphology of the samples. RS, UV–vis DRS, and XPS results indicated enhanced oxygen vacancies in the Y doped samples. H_2-TPR profiles confirmed a facile reduction of CZY and CLY samples at lower temperatures. BET analysis revealed an enhanced surface area for CZY and CLY samples than the respective CZ and CL undoped mixed oxides. All these factors contributed to a better CO and soot oxidation performance of CZY and CLY samples. Particularly, the CLY sample exhibited highest catalytic activity among the various samples investigated.

Graphical Abstract

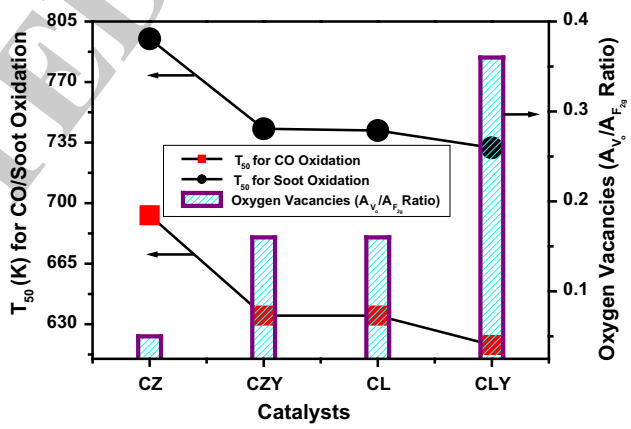

Keywords Ternary oxides · Solid solutions · Oxygen vacancies · CO oxidation · Soot oxidation

D. Devaiah · B. M. Reddy (✉)
Inorganic and Physical Chemistry Division, CSIR–Indian Institute of Chemical Technology, Uppal Road, Hyderabad 500 007, India
e-mail: bmreddy@iict.res.in

D. Devaiah · T. Tsuzuki
Research School of Engineering, Australian National University, Canberra, ACT 0200, Australia

C. U. Aniz
R&D Division, Sud-Chemie India Pvt. Limited, Binanipuram 683502, Kerala, India

1 Introduction

Carbon monoxide and soot are serious pollutants generated by various combustion processes, causing worldwide problems to our environment. Hence, catalytic oxidation of these pollutants is a promising avenue both technologically and scientifically to overcome the problem [1, 2]. Ceria (CeO_2) is well recognised as one of the most efficient oxidising catalysts due to its unique oxygen storage

Journal : Large 10562 | Dispatch : 3-3-2015 | Pages : 11
Article No. : 1507 | LE | TYPESET
MS Code : CATLET-2014-1114 | CP | DISK

capacity (OSC), outstanding redox property, and abundant oxygen-vacancy defects [3–5].

Despite many merits, there are several disadvantages associated with pristine ceria. CeO_2 mainly suffers from poor thermal stability and low specific surface area thereby limited oxygen vacancies which retard the elevated temperature activity demands for catalytic applications. As a solution, different transition and rare-earth metal ions were doped into the ceria cubic structure and the resulting materials were investigated systematically with an aim to overcome the disadvantages of pure CeO_2 [6–10]. Formation of dopant incorporated ceria-based solid solutions normally modifies the structural, textural, redox, and catalytic properties of ceria. It has been widely established that the properties of CeO_2 could be significantly improved by the incorporation of Zr^{4+} cations, and the resulting $Ce_xZr_{1-x}O_2$ (CZ) solid solution was found to show an excellent catalytic activity for various oxidation reactions [11, 12]. For instance, Fornasiero et al. reported that the reduction behaviour of CeO_2 significantly improves by Zr doping [13]. Thammachart et al. also reported that cubic phase $Ce_{0.75}Zr_{0.25}O_2$ solid solution with high reducibility exhibits good catalytic activity for CO oxidation [14]. Atribak et al. studied the effect of ZrO_2 doping on the catalytic activity of CeO_2 and indicated that Zr^{4+} doping greatly enhance the catalytic ability for soot oxidation [12]. Aneggi et al. also showed an improved oxidation of soot particles by surface active oxygens donated by different compositions of CZ solid solutions [15].

A similar strategy to enhance the catalytic activity of CeO_2 was explored by employing lanthanum as an additive into the ceria lattice and producing ceria–lanthana (CL) solid solution. Extensive work from our group confirmed an enhanced soot and CO oxidation activity over CL solid solutions in comparison to CZ [8, 16].

Propitiously, it has been found that the catalytic performance of CeO_2-based binary oxide solid solutions was further improved upon the introduction of additional transition or rare earth (RE) cation dopants [17, 18]. For example, Hari Prasad and co-workers have investigated the influence of RE dopants on the catalytic properties of CZ solid solutions for CO oxidation [19]. They confirmed that $Ce_{0.65}Zr_{0.25}RE_{0.1}O_{2-\delta}$ exhibits superior catalytic activity compared to undoped $Ce_{0.75}Zr_{0.25}O_{2-\delta}$ solid solution. Various transition metal (Fe, Co) ion doped CZ solid solutions showed improved OSC which promote the catalytic performance of supported Pd-only three-way catalysts in automotive emission control applications [20]. Very recently, our group also reported that incorporation of Hf, Pr, and Tb cations into the CZ solid solution shows better catalytic activity towards CO oxidation in comparison to undoped sample [21]. The trivalent cation dopants (e.g., La^{3+}, Y^{3+}, or Pr^{3+}) are expected to improve the OSC and redox ability of CZ solid solutions [22]. Interestingly, Y^{3+} cation has been proven to be one of the good dopants to improve the catalytic activity of CZ solid solutions for soot oxidation [23]. He et al. showed that the addition of small amounts of Y^{3+} to Zr^{4+} doped RE (RE = Ce, Pr) oxides results in the formation of $RE_{0.6}Zr_{0.35}Y_{0.05}O_2$ ternary oxide solid solutions with improved oxygen vacancies, lattice oxygen mobility, OSC, and redox properties than undoped $RE_{0.6}Zr_{0.4}O_2$ (RE = Ce, Pr) binary oxide solid solutions [24–26]. However, to date, there are only a few reports concerning the development of CeO_2–La_2O_3–Y_2O_3 (CLY) ternary oxide solid solutions for catalytic applications.

These results have led us to think that Y^{3+} is an ideal dopant that could improve the textural and structural properties of ceria–zirconia and ceria–lanthana solid solutions for oxidation reactions. Thus, the present study mainly aimed to understanding the influence of Y dopant on the structural, textural, and redox properties of ceria–zirconia and ceria–lanthana solid solutions for CO and soot oxidations. Accordingly, we have prepared Y^{3+} doped Ce–Zr–O and Ce–La–O solid solutions by a facile coprecipitation method. Undoped Ce–Zr–O and Ce–La–O solid solutions and pure CeO_2 were also prepared for comparison. The physicochemical properties of the prepared samples were characterized by means of XRD, ICP–OES, Raman, UV–vis DRS, XPS, H_2-TPR, HREM, and BET SA techniques.

2 Experimental

2.1 Catalyst Preparation

Y-doped ceria–zirconia and ceria–lanthana samples with the optimized composition of $Ce_{0.8}Zr_{0.12}Y_{0.08}O_{2-\delta}$ (thereafter denoted as CZY) and $Ce_{0.8}La_{0.12}Y_{0.08}O_{2-\delta}$ (thereafter denoted as CLY) were prepared via a simple coprecipitation method. $Ce(NO_3)_3{\cdot}6H_2O$, $ZrO(NO_3)_2{\cdot}xH_2O$, $La(NO_3)_3{\cdot}6H_2O$, and $Y(NO_3)_3{\cdot}6H_2O$ were used as the metal precursors. Firstly, an appropriate amount of these metal precursors were dissolved in deionized water and mixed together with vigorous stirring for 30 min. Subsequently, excess aqueous NH_3 solution was slowly dropped into the above mixed solution until the pH reached ~8.5. The resulting suspension was kept stirring for another 12 h, aged for 24 h and then filtered and washed several times with distilled water until free from anion impurities. The obtained precipitates were oven dried overnight at 373 K, followed by calcination at 773 K for 5 h at a heating rate of 5 K min^{-1}. The reference pure ceria, ceria–zirconia (hereafter denoted as CZ), and ceria–lanthana (hereafter denoted as CL) solid solutions were also prepared by adopting the same method for comparison.

Journal : Large 10562 Dispatch : 3-3-2015 Pages : 11
Article No. : 1507 LE TYPESET
MS Code : CATLET-2014-1114 CP DISK

2.2 Catalyst Characterization

X-ray diffraction measurements were performed on a Rigaku Multiflex diffractometer equipped with a nickel-filtered Cu-Kα (1.5418 Å) radiation source and a scintillation counter detector. The diffraction patterns were recorded over a 2θ range of 10–80° with a 0.021 step size and using a counting time of 1 s per point. The XRD phases present in the samples were identified with the help of Powder Diffraction File from the International Centre for Diffraction Data (PDF-ICDD). The mean crystallite size (D) was measured by applying the Scherrer equation. The lattice parameter was calculated by a standard cubic indexation method with the intensity of most prominent peaks using the relation $a = d(h^2 + k^2 + l^2)^{1/2}$ where a is the lattice parameter and d is the interplanar spacing calculated from Bragg equation.

The chemical analysis of the prepared samples was performed by inductively coupled plasma optical emission spectroscopy (ICP–OES, Thermo Jarrel Ash model IRIS Intrepid II XDL, USA) to confirm the respective concentration of elements in the system. For ICP analysis, approximately 50 mg of the sample was dissolved in a solution of 25 mL aqua regia and 475 mL distilled water. Then 10 mL of the above solution was diluted to 250 mL.

Raman spectra were obtained at room temperature using a LabRam HR800UV Raman spectrometer (Horiba Jobin–Yvon) fitted with a confocal microscope and liquid-nitrogen cooled charge-coupled device (CCD) detector. Samples were excited with the emission line at 632 nm from an Ar^+ ion laser (Spectra Physics) which was focused on the sample under the microscope with the diameter of the analyzed spot being ~1 μm. The acquisition time was adjusted according to the intensity of Raman scattering. The wavenumber values obtained from the spectra are precise to within 2 cm^{-1}. UV–vis DRS measurements were performed by using a GBSCintra 10e UV–vis NIR spectrophotometer with an integration sphere diffuse reflectance attachment. $BaSO_4$ was used as the reference and spectra were recorded in the range 200–800 nm.

XPS measurements were performed on a Shimadzu ESCA 3400 spectrometer using Mg–Kα (1253.6 eV) radiation as the excitation source at room temperature. The samples were maintained in a strict vacuum typically on the order of less than 10^{-8} Pa to avoid a large amount of noise in the spectra from contaminants. The obtained binding energies were corrected by referencing the spectra to the carbon (C 1s) peak at 284.6 eV.

The reducibility of the catalysts was studied by H_2-TPR analysis using a thermal conductivity detector of a gas chromatograph (Shimadzu). Prior to the reduction, approximately 30 mg of the sample was loaded in an isothermal zone of the reactor and pre-treated in a helium gas flow at 473 K and then cooled to room temperature. Then, the sample was heated at a rate of 10 K min^{-1} from ambient temperature to 1100 K in a 20 mL min^{-1} flow of 5 % H_2 in Ar. The hydrogen consumption during the reduction process was estimated by passing the effluent gas through a molecular sieve trap to remove the produced water and was analyzed by a gas chromatography using the thermal conductivity detector.

Transmission electron microscopy studies were carried out on a JEM-2100 (JEOL) microscope equipped with a slow-scan CCD camera at an accelerating voltage of 200 kV. Samples for TEM analysis were prepared by crushing the materials in an agate mortar and dispersing them ultrasonically in ethyl alcohol for 5 min. Afterward a drop of the dilute suspension was placed on a perforated-carbon-coated copper grid and allowed to dry by evaporation at ambient temperature. BET surface areas were determined by N_2 physisorption at liquid N_2 temperature on a Micromeritics Gemini 2360 instrument using a thermal conductivity detector. Prior to analysis, the samples were degassed at 393 K for 2 h to remove the surface adsorbed residual moisture.

2.3 Catalytic Activity Studies

CO oxidation reaction was studied with the catalysts granulated to 1 mm mesh size after shaping to cylindrical tablets. About 0.3 g of the catalyst was supported between glass wool plugs and flanked by inert porcelain beads in the middle of a specially designed quartz reactor. The samples were activated in air at 573 K for 1 h prior to the reaction studies. The inlet gas was a calibrated mixture of 5 % O_2, 1 % CO in N_2. Gas flow was adjusted to a space velocity of 30,000 h^{-1}. The composition of the gas exiting the reactor was monitored by a gas chromatography.

Catalytic activity for soot oxidation was determined by a thermogravimetric (TG) method with a Mettler Toledo, TGA/SDTA 851^e instrument. Activity measurements were performed with O_2 in ''tight contact'' (ground in agate mortar) conditions with catalyst–soot mixtures in 4:1 *w*/*w* ratio. The model soot, Printex U, used in this work was provided by Degussa. A weighed amount of sample was placed in a TG crucible and the oxidation experiments consisted of heating the soot–catalyst mixtures at 10 K min^{-1} from RT to 1273 K in 100 mL min^{-1} flow of air.

3 Results and Discussion

3.1 Characterization Studies

Figure 1 displays the X-ray diffraction patterns of pure CeO_2, undoped (CZ and CL), and Y-doped CZ and CL

Journal : Large 10562 | Dispatch : 3-3-2015 | Pages : 11
Article No. : 1507 | LE | TYPESET
MS Code : CATLET-2014-1114 | CP | DISK

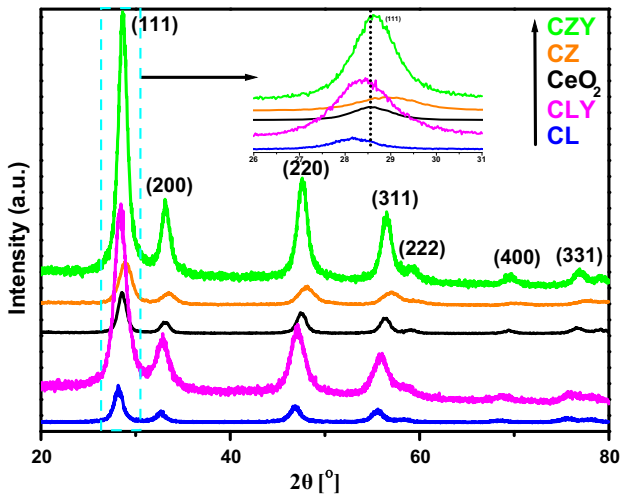

Fig. 1 Powder X-ray diffraction patterns of pure CeO_2, undoped and Y-doped ceria–zirconia and ceria–lanthana solid solutions (*inset* expanded view of selected region)

(CZY and CLY) samples calcined at 773 K. For all samples, the XRD phase analysis showed only the presence of single phase cubic CeO_2 fluorite structure (PDF-ICDD 34-0394) without extra characteristic lines associated with ZrO_2, La_2O_3 and Y_2O_3. However, in comparison to pure CeO_2, the (111) reflection in the diffraction patterns of CZ is slightly shifted to higher angle side, while it is slightly shifted to lower angle side in the case of CL sample (Table 1 and enlarged view in Fig. 1). These changes can be attributed to the formation of CZ and CL solid solutions with the replacement of Ce^{4+} (0.97 Å) ions by the smaller Zr^{4+} (0.84 Å) and larger La^{3+} (1.17 Å) ions, respectively. Interestingly, the (111) peak position of CZ and CL is slightly shifted towards lower and higher angle side, respectively, upon doping with the Y^{3+} (1.04 Å) ions (shown in Table 1 and enlarged view of Fig. 1). This result supports the formation of uniform CZY and CLY solid solutions by successful incorporation of Y^{3+} ions into the lattices of CZ and CL, respectively.

As shown in Table 1, the lattice parameter of CZ is decreased to 0.5354 nm from 0.5415 nm of pure CeO_2, while it increased to 0.5488 nm for CL. This phenomenon could be associated with the contraction and expansion of CZ and CL crystal lattices, respectively, which is induced owing to the smaller (Zr^{4+}) and larger (La^{3+}) cation radius of the dopants relative to the Ce^{4+} ion. Furthermore, the calculated lattice parameter of CZY (0.5392 nm) is greater than that of CZ (0.5354 nm). This finding is consistent with the lattice expansion due to the larger ionic radius of Y^{3+} than the Zr^{4+} dopant, since it could replace the Ce^{4+} ions during the formation of CZY solid solution. On the other hand, the lattice parameter of CLY is smaller than that of CL (Table 1), which is primarily due to the fact that the ionic radius of Y^{3+} is smaller than that of La^{3+} dopant. Therefore, the incorporation of Y^{3+} into the lattice of CeO_2 leads to contraction of the lattice. The doping of Y^{3+} ions thus likely induced the distortion of the CZ and CL lattices, enhancing the oxygen vacancies in CZY and CLY samples, respectively. These results again confirm the formation of solid solutions. The crystallite sizes of all samples are found to be 5–8 nm. The elemental composition of the CZY and CLY samples were confirmed by ICP–OES technique (Table 2).

Raman spectroscopy is an effective tool to detect the changes in the vibrational structure of CeO_2 caused by the doping which supports some of the conclusions drawn from XRD analysis [27]. The information on metal–oxygen bond arrangement and/or oxygen vacancies thereby relative OSC of CeO_2-based oxides can be obtained by Raman spectroscopy [28]. Figure 2 demonstrates the Raman spectra of all samples. The spectrum of pure CeO_2 exhibited a most prominent peak at 465 cm^{-1}, which can be attributed to the F_{2g} vibration of the fluorite-type structure. This mode further corresponds to the symmetric vibration of oxygen ions around Ce^{4+} ions in the CeO_8 octahedra which is very sensitive to any disorder in oxygen sublattice [29]. The peak positions of CZ and CL samples shifted to higher and lower frequencies, respectively, when compared to the peak position of pure CeO_2 (Table 1). These shifts can be ascribed to the lattice contraction and expansion related to the replacement of Ce^{4+} (0.97 Å) with smaller Zr^{4+} (0.84 Å) and larger La^{3+} (1.17 Å) ions, respectively. In addition, the main band showed a shift towards lower energies in CZY compared to CZ, indicating that the cell

Table 1 The physical and chemical properties of investigated samples

Sample	2θ	Crystallite size (nm)	Lattice parameter (nm)	BET SA (m^2/g)	F_{2g} (cm^{-1})	$A_{V_0}/A_{F_{2g}}$	$[Ce^{3+}]/[Ce^{3+} + Ce^{4+}]$ %
CeO_2	28.56	7.3	0.5415	41	465.2	–	25.8
CZ	28.98	4.7	0.5354	84	475.6	0.05	41.7
CZY	28.65	7.6	0.5392	115	462.6	0.16	43.7
CL	28.18	8.3	0.5488	66	448.1	0.16	43.5
CLY	28.40	5.6	0.5436	123	453.3	0.36	45.5

Journal : Large 10562 Dispatch : 3-3-2015 Pages : 11
Article No. : 1507 LE TYPESET
MS Code : CATLET-2014-1114 CP DISK

Table 2 The elemental composition and surface atomic ratios of investigated samples

Sample	Nominal composition				Elemental composition from ICP–OES analysis				Surface atomic ratios from XPS			
	Ce	Zr	La	Y	Ce	Zr	La	Y	Ce/Zr	Ce/La	Ce/Zr + Y	Ce/La + Y
CZ	–	–	–	–	–	–	–	–	0.90	–	–	–
CZY	0.80	0.12	–	0.08	0.78	0.13	–	0.09	–	–	1.38	–
CL	–	–	–	–	–	–	–	–	–	1.35	–	–
CLY	0.80	–	0.12	0.08	0.78	–	0.13	0.09	–	–	–	1.67

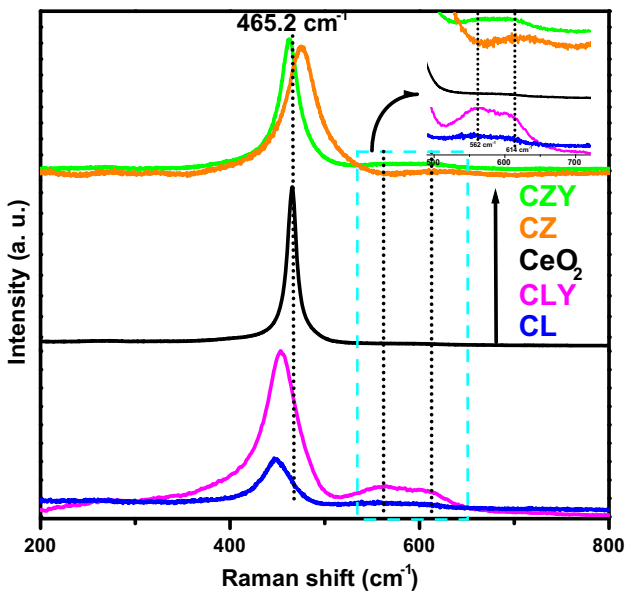

Fig. 2 Raman spectra of pure CeO_2, undoped and Y-doped ceria–zirconia and ceria–lanthana solid solutions (*inset* expanded view of selected region)

expansion due to Y^{3+} (1.04 Å) doping slightly prevails with regard to the contraction due to Zr^{4+} doping. On the other hand, doping of Y^{3+} ions into CL resulted in an increase of the peak position, which implies lattice contraction in the CLY induced by the incorporation of smaller Y^{3+} ions than the La^{3+} dopant into the CeO_2. Therefore, the changes in lattice parameter values as measured from XRD explain the Raman shifts very well [29]. Further, the shift of F_{2g} mode from 465 cm^{-1} clearly suggests the formation of solid solutions, which is again in good agreement with the XRD results [28].

Besides the F_{2g} mode, the Raman spectra of CL, CLY, CZY samples showed two additional modes at ~562 and ~614 cm^{-1}. On the other hand, for CZ sample, only one additional band appeared at ~614 cm^{-1} (inset of Fig. 2). These modes are related to the local vibrations of different oxygen vacancies (V_o). The ~562 cm^{-1} band is ascribed to extrinsic oxygen vacancies introduced into the CeO_2 in order to maintain charge neutrality when Ce^{4+} ions are replaced with trivalent cations such as La^{3+} and/or Y^{3+}. Further, the mode at ~614 cm^{-1} originates from the existence of intrinsic oxygen vacancies due to the Ce^{3+} ions, which can be created by the substitution of Ce^{4+} ions with different size dopants (Zr^{4+}, La^{3+}, Y^{3+}) [30, 31]. The ratio between the peak areas of V_0 (A_{V_0}) and F_{2g} ($A_{F_{2g}}$) reflects the relative concentration of oxygen vacancies which can be directly linked to the OSC of the materials [28]. The calculated $A_{V_0}/A_{F_{2g}}$ values of the samples were listed in Table 1. The $A_{V_0}/A_{F_{2g}}$ ratio for pure CeO_2 was not calculated due to the negligible intensity of oxygen vacancy peak. It could be observed from Table 1, the $A_{V_0}/A_{F_{2g}}$ values of the samples are ranked in the order: CLY > CZY ≈ CL > CZ. The result suggests that the amount of oxygen vacancies in CZ and CL were significantly enhanced upon doping with Y^{3+} ions, which is important for catalytic reactions and particularly for enhancing the CO and soot oxidation activity. CLY sample showed an improved concentration of oxygen vacancies than CZY. This implies that the different ionic radius and oxidation states of both La^{3+} and Y^{3+} dopants compared to that of Ce^{4+} increased the two kinds of oxygen vacancies in CeO_2 lattice. Conversely, in the case of CZY samples, since Zr^{4+} ion is isovalent with Ce^{4+}, only Y^{3+} dopant can enhance the two types of oxygen vacancies. The $A_{V_0}/A_{F_{2g}}$ value of CZ was lower than that of CL. Due to the different ionic radius and oxidation state of La^{3+} dopant than Ce^{4+}, two types of oxygen vacancies were generated in CL sample. On the contrary, in CZ, Zr^{4+} is isovalent with Ce^{4+} and hence only intrinsic oxygen vacancies were created owing to different ionic size of Zr^{4+} than Ce^{4+}.

The UV–vis DR spectra of pure CeO_2, undoped (CZ and CL) and Y-doped CZ and CL (CZY and CLY) samples are displayed in Fig. 3. The broad absorption band is observed for all samples in the 225–480 nm region which could be due to the charge-transfer transition from the O 2p to Ce 4f orbitals in CeO_2. According to the literature, pure CeO_2 shows three distinct absorption peaks at ~255, ~285, and ~340 nm which are assigned to $O^{2-} \rightarrow Ce^{3+}$ and $O^{2-} \rightarrow Ce^{4+}$ charge transfer (CT), and interband (IB) transitions, respectively [32]. Therefore, the broad band of

Journal : Large 10562 Dispatch : 3-3-2015 Pages : 11
Article No. : 1507 LE TYPESET
MS Code : CATLET-2014-1114 CP DISK

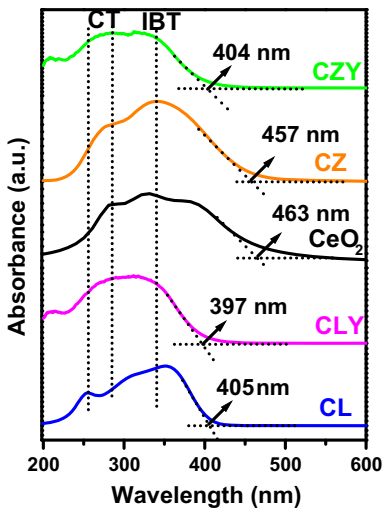

Fig. 3 UV-visible DR spectra of pure CeO_2, undoped and Y-doped ceria–zirconia and ceria–lanthana solid solutions

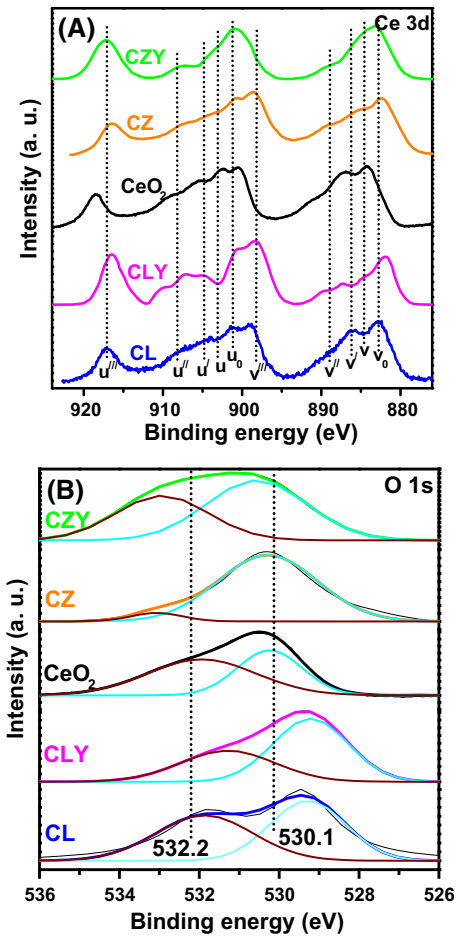

Fig. 4 XP spectra of **a** Ce 3d **b** O 1s for pure CeO_2, undoped and Y-doped ceria–zirconia and ceria–lanthana solid solutions

all samples can be attributed to the overlap of CT and IB transitions, indicating the coexistence of Ce^{3+} and Ce^{4+} ions in the samples. Furthermore, the absorption bands of ZrO_2, La_2O_3 and Y_2O_3 are not detected during the UV–vis DRS experiment, indicating the formation of solid solutions which is in agreement with XRD and Raman analysis. Interestingly, Y-doping into CZ and CL caused a blue shift in the absorption edge. The reason may be that the Y-doping induced a significant increase in the Ce^{3+} fraction (oxygen vacancies) on the surface compared with the undoped CZ and CL samples which leads to an increase in the charge-transfer gap between O 2p and Ce 4f orbitals and consequently the blue-shift of absorption spectrum for CZY and CLY [9]. CLY exhibited a blue shift more prominently than CZY, indicating the higher oxygen vacancy concentration in CLY than in CZY. Moreover, similar absorption edges of CZY and CL may suggest similar concentrations of oxygen vacancies in the two samples. These results are strongly consistent with the Raman measurements.

To identify the surface composition and oxidation states of the elements, X-ray photoelectron spectroscopy characterization is performed in the Ce 3d, Zr 3d, La 3d, Y 3d, and O1s regions. The Ce 3d XPS patterns of CeO_2, CZ, CL, CZY, and CLY samples are shown in Fig. 4a. For all samples, it can be found that the Ce 3d level exhibited ten peaks which correspond to five pairs of spin–orbit doublets of $3d_{5/2}$ and $3d_{3/2}$, labelled as v_0, v, v′, v″, v‴ and u_0, u, u′, u″, u‴ peaks, respectively. The peaks of u_0, u′, v_0, and v′ are assigned to Ce^{3+} species, whereas the u, u″, u‴, v, v″, and v‴ peaks are characteristic of Ce^{4+} species [32–34]. These observations clearly indicate the coexistence of Ce^{3+} and Ce^{4+} species on the surface of all samples.

More importantly, the presence of Ce^{3+} is associated with the formation of oxygen vacancies which are closely linked with OSC [28, 35]. In order to estimate the quantity of surface oxygen vacancies, the relative concentration of Ce^{3+} ions was calculated from the integrated areas (A_i) of the respective peaks as $[Ce^{3+}]/[Ce^{3+} + Ce^{4+}] = (A_{u0} + A_u' + A_{v0} + A_v')/(A_u + A_u'' + A_u''' + A_v + A_{v-} + A_v''')$ [36]. The calculation results were listed in Table 1. It can be seen that the relative concentration of Ce^{3+} ions for CeO_2, CZ, CL, CZY, and CLY follows the sequence: CLY (45.5 %) > CZY (43.5 %) ≈ CL (43.7 %) > CZ (41.7 %) > CeO_2 (25.8 %). This order demonstrates that CZ and CL have more oxygen vacancies than pure CeO_2. Interestingly, the concentration of oxygen vacancies was further increased after doping of Y into CZ and CL. In addition, CZY had a lower amount of oxygen vacancies than CLY and showed a similar quantity of oxygen vacancies to that of CL. These observations strongly support the conclusions drawn from Raman spectroscopy. The higher oxygen vacancy concentration of

Journal : Large 10562 Dispatch : 3-3-2015 Pages : 11
Article No. : 1507 ☐ LE ☐ TYPESET
MS Code : CATLET-2014-1114 ☑ CP ☑ DISK

CLY would be greatly benefited for the higher activity in CO and soot oxidation.

The O 1s XP spectra of all samples are depicted in Fig. 4b, which is mainly composed of two components. The main peak detected at 529.2–530.5 eV is related to the lattice oxygen of the metal oxides. The distinct shoulder peak at the higher binding energy (531.3–533.2 eV) is attributed to surface carbonates, hydroxyl groups, surface oxygen ions, and water [9, 28].

The Zr 3d XP spectra of CZ and CZY samples are presented in Fig. 5a. It could be observed that two peaks at ~182.3 and ~184.7 eV is attributed to the Zr $3d_{5/2}$ and Zr $3d_{3/2}$ levels, respectively. The splitting energy between these two components is calculated to be approximately 2.4 eV, which is in agreement with the literature [37]. From the La 3d core level spectra of CL and CLY samples (Fig. 5b), it could be seen that four peaks at ~834.3 and ~838.4, and ~851 and ~855.2 eV are related to La $3d_{5/2}$ and La $3d_{3/2}$ levels, respectively. The splitting in La $3d_{5/2}$ and La $3d_{3/2}$ levels is due to spin orbit interaction and charge transfer from O 2p to La 4f. Moreover, the observed difference in $3d_{5/2}$ and $3d_{3/2}$ binding energies is ~4.1–4.2 eV, which is well supported by the previous reports [8]. The XPS pattern of Y 3d of CZY and CLY samples is further illustrated in Fig. 5c and it consists of an asymmetrical peak that could be decomposed to two components at binding energies ~157.1 and ~159.2 eV. The peaks at the higher and lower binding energies can be assigned to Y $3d_{3/2}$ and Y $3d_{5/2}$, respectively [38]. The results reveal that the La and Y ions are present in 3+ states whereas Zr is in 4+ oxidation state. The calculated atomic ratios at the surface of the samples are also listed in Table 2. The obtained atomic ratios clearly indicated the enrichment of the dopants at the surface region of the

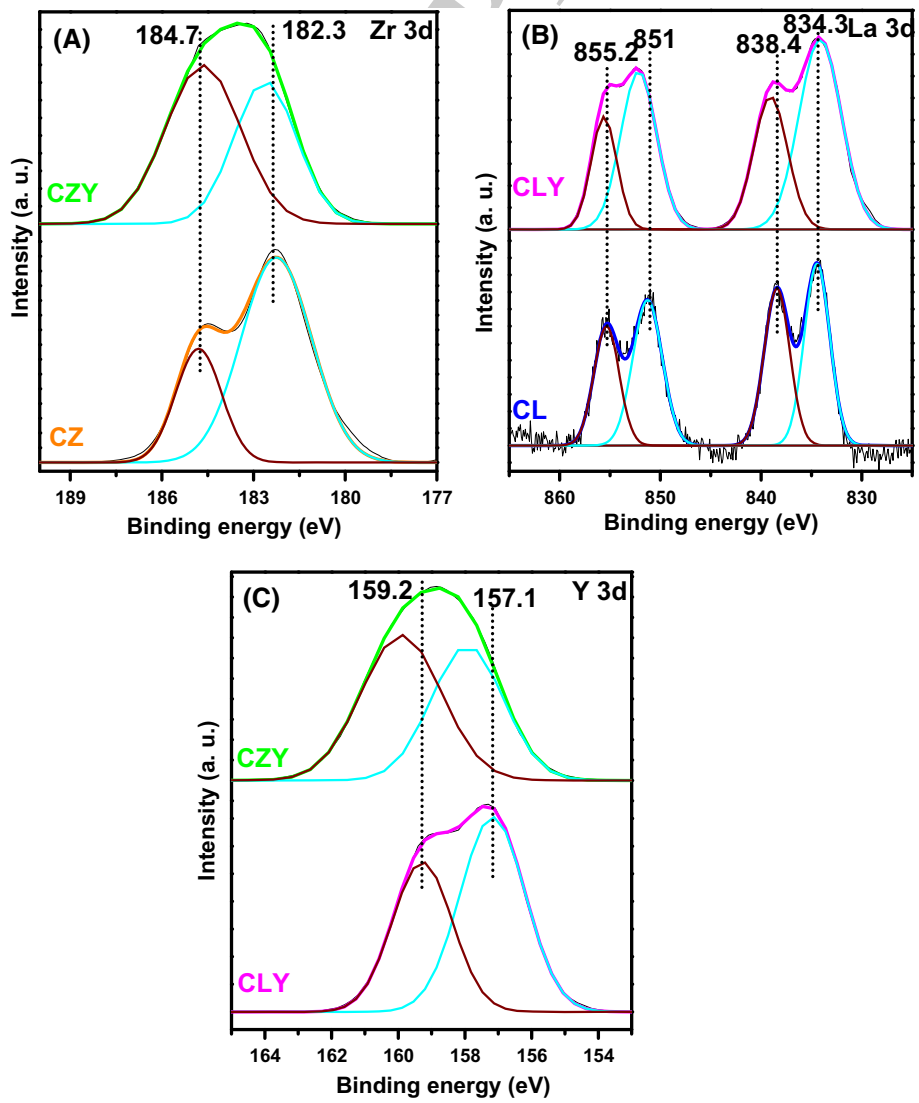

Fig. 5 XP spectra of **a** Zr 3d for undoped and Y-doped ceria–zirconia solid solutions, **b** La 3d for undoped and Y-doped ceria–lanthana solid solutions, **c** Y 3d for Y-doped ceria–zirconia and ceria–lanthana solid solutions

Journal : Large 10562 | Dispatch : 3-3-2015 | Pages : 11
Article No. : 1507 | LE | TYPESET
MS Code : CATLET-2014-1114 | CP | DISK

samples. The highest atomic ratio of Ce/dopant(s) can be found on the surface of CLY (1.67), followed by CZY (1.38), CL (1.35), and CZ (0.9).

The reducibility of all the samples was evaluated by H_2-TPR experiments and the profiles obtained are compiled in Fig. 6. It is important to notice that the H_2 consumption must be attributed to Ce^{4+} reduction, since Zr^{4+}, La^{3+}, and Y^{3+} ions are hardly reduced. However, the Zr^{4+}, La^{3+}, and Y^{3+} dopants can modify the reduction behaviour of CeO_2. Pure CeO_2 presents the well-known profile consisting of a surface reduction peak at ~755 K and a bulk reduction peak at ~1005 K [27, 39]. With the doping of Zr^{4+} and La^{3+} ions, the bulk peak intensified and shifted to lower temperatures from ~1005 K for the pure CeO_2 to ~845 K and ~829 K for CZ and CL, respectively. Moreover, compared with pure CeO_2, the surface reduction of CZ is negligible, whereas for CL it shows a less intense peak. These results suggest that Zr^{4+} and La^{3+} doping definitely favors the bulk reduction at a lower temperature than for pure CeO_2.

It could be clearly observed from Fig. 6 that CZY and CLY exhibited different TPR profiles than that of CZ and CL, respectively. Interestingly, the CLY sample shows only one reduction peak at ~570 K which may be due to the concurrent reduction of surface and bulk of the sample. In addition, the reduction temperature of CLY is obviously much lower than the CZY and all other samples. The generally accepted argument to explain this type of behaviour is that the creation of oxygen vacancies by the removal of surface oxygen atoms during the reduction process. As a result, concurrently bulk oxygen atoms move to the surface and oxygen vacancies progress in the opposite direction. As is known from Raman and XPS results, the oxygen vacancies are greatly enhanced by the Y-doping into CL lattice and consequently, boost up the mobility of oxygen in the lattice which can facilitate easier reduction of CeO_2 in CLY sample [27]. Therefore, the presence of La and Y in CLY is beneficial for the easy formation of oxygen vacancies which are important for catalytic reactions.

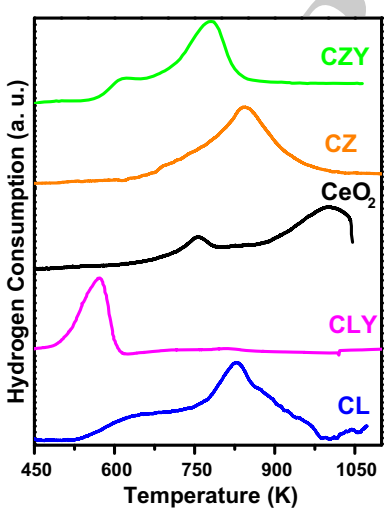

Fig. 6 H_2-TPR profiles of pure CeO_2, undoped and Y-doped ceria–zirconia and ceria–lanthana solid solutions

The TEM technique is performed to ascertain the morphology and crystallite growth of the samples. Figure 7 displays the HRTEM images of CZ, CL, CZY, and CLY samples. It could be observed that all the samples are composed of irregular shapes with well-defined crystal facets of the particles. Further, the statistical analysis of the images revealed the average grain size of these samples is in the range of 4.8–8.6 nm, which is in good agreement with the results of XRD. The lattice fringes of all samples are clearly visible with a *d* spacing of 0.308, 0.315, 0.311, and 0.310 nm for CZ, CL, CZY, and CLY, respectively. This is attributed to the (111) plane of CeO_2, indicating that the most frequently exposed crystal plane of these samples should be the (111) plane.

3.2 Activity Studies

3.2.1 CO Oxidation

The catalytic activities for CO oxidation of all samples are presented in Fig. 8. As expected, the CO conversion increases with increasing reaction temperature for all samples. The activity of samples is evaluated by the T_{50} (the reaction temperature for 50 % CO conversion) and corresponding values are summarized in Table 3. It can be seen that the T_{50} values for the CZ (693 K) and CL (635 K) are lower than that of the pure CeO_2 (714 K), indicating that the CZ and CL samples exhibit a better activity towards CO oxidation. For Y-doped CZ and CL samples, the T_{50} value is 618 K for the CLY and 635 K for the CZY, suggesting that the incorporation of Y further improves the catalytic performance for CO oxidation. It is also evident that the CLY sample shows higher catalytic activity compared to the CZY sample and the activity of CZY is similar to that of CL sample. In other words, at the T_{50} temperature of CLY, the CZY, CL, CZ, and CeO_2 samples exhibited only 35, 35, 17, and 13.5 % conversions, respectively (Table 3). Hence, the sequence of catalytic activity expressed as CO conversion is as follows: CLY > CZY ≈ CL > CZ > CeO_2. Interestingly, the difference in T_{50} between CZY and CZ is very high (58 K) compared to that between CLY and CL which is only 17 K. This result clearly indicates that the Y^{3+} dopant significantly effects on the activity of CZ than on the CL.

In general, the catalytic activity of the materials is related to their surface areas since catalysts with higher BET surface areas often exhibit higher catalytic activities. As shown in Table 1, the BET surface areas of the samples are

Journal : Large 10562 | Dispatch : 3-3-2015 | Pages : 11
Article No. : 1507 | LE | TYPESET
MS Code : CATLET-2014-1114 | CP | DISK

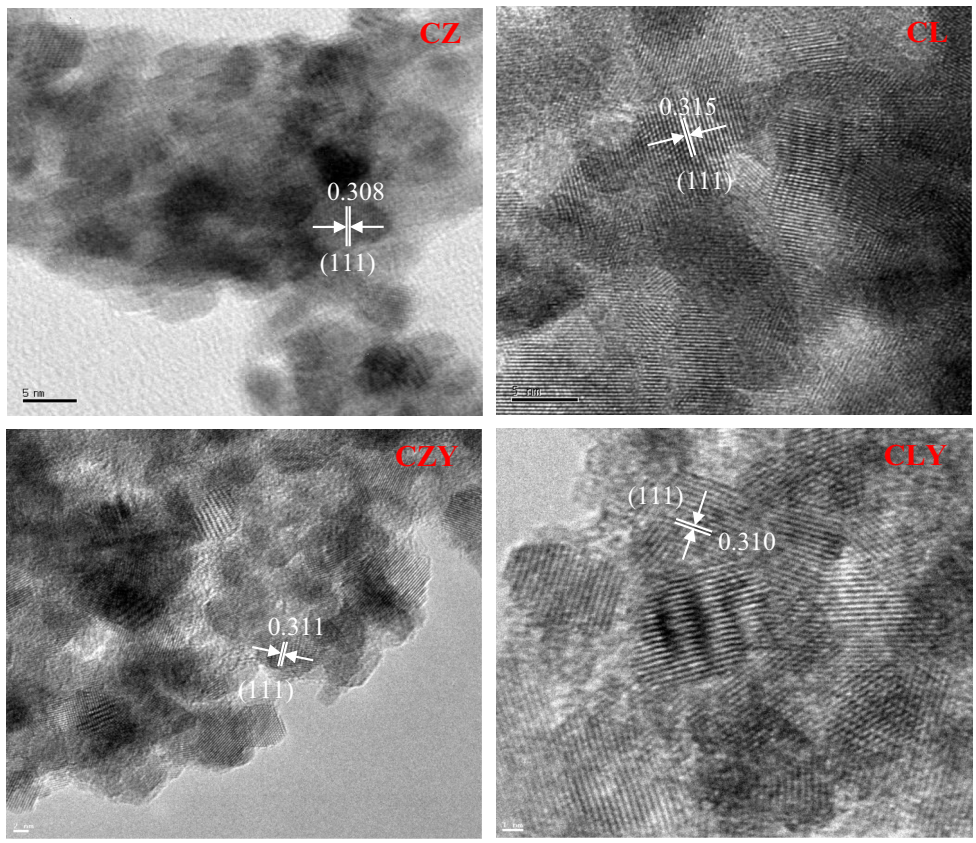

Fig. 7 HRTEM images of undoped and Y-doped ceria–zirconia and ceria–lanthana solid solutions

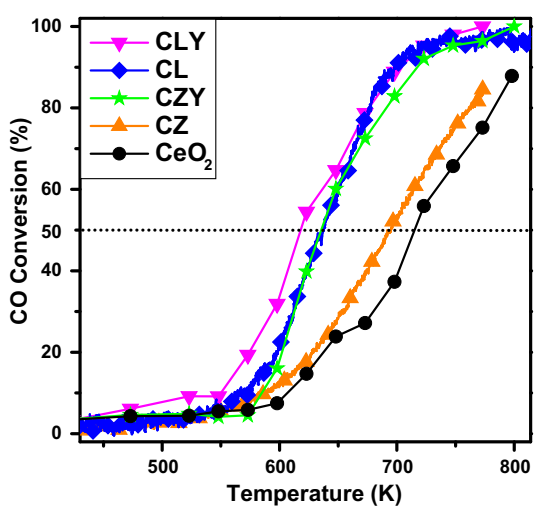

Fig. 8 Catalytic activity of pure CeO_2, undoped and Y-doped ceria–zirconia and ceria–lanthana solid solutions for CO oxidation

123, 115, 84, 66, and 41 $m^2\ g^{-1}$ for CLY, CZY, CZ, CL, and CeO_2, respectively. From these results it could be concluded that the Y dopant greatly enhance the surface area of CZ and CL samples compared to the undoped CZ and CL samples, respectively. The CLY sample with the highest surface area exhibited the best catalytic activity among the samples. However, the CZY and CL samples have similar activity (based on T_{50}) and yet showed obvious differences in their surface areas. Moreover, the CL sample shows higher activity than CZ although it has lower surface area than the CZ sample. Therefore, the order of BET surface areas of our samples is not consistent with the order of activity, implying that the surface area may not be the crucial factor determining the catalytic activity for CO oxidation.

Generally, for CO catalytic oxidation over CeO_2, the reaction proceeds via the Mars–Van Krevelen mechanism [8]. Firstly, CO is adsorbed on the catalyst surface through coupling with the adjacent Ce^{3+} ions, since they serve as effective binding sites for CO adsorption. Then, these adsorbed CO molecules are oxidized by the surrounding lattice oxygen atoms, leading to oxygen vacancy creation; after that, gas-phase O_2 reacts with the reduced surface to regenerate the surface oxygen atom. However, Ce^{3+} ions are exclusively exposed by the presence of oxygen vacancies. Therefore, the number of oxygen vacancies to adsorb the CO molecules should be an important factor in determining the tendency for CO oxidation. This means that the sample with more oxygen vacancies could provide more Ce^{3+} adsorption sites to interact with CO and have higher catalytic activities. From Raman and XPS analyses,

Journal : Large 10562 | Dispatch : 3-3-2015 | Pages : 11
Article No. : 1507 | LE | TYPESET
MS Code : CATLET-2014-1114 | CP | DISK

Table 3 Catalytic performance for CO and soot oxidation over investigated samples

Sample	T_{50} (CO) (K)[a]	C_{co} (618 K) (%)[b]	T_{50} (Soot) (K)[c]	C_{Soot} (732 K) (%)[d]
CeO_2	714	13.5	876	9.6
CZ	693	17	796	18.9
CZY	635	35	743	44.4
CL	635	35	742	44.4
CLY	618	50	732	50

[a] The temperature for CO 50 % conversion

[b] CO conversion at the 50 % conversion temperature of CLY

[c] The temperature for Soot 50 % conversion

[d] Soot conversion at the 50 % conversion temperature of CLY

the concentration of oxygen vacancies for all samples is calculated and it is consistent with the above observed activity order. In addition, the H_2-TPR experiment discloses the enhanced reducibility and oxygen mobility for CLY sample. Therefore, the oxygen vacancies can be responsible for the catalytic CO oxidation reaction and particularly, superior performance of CLY sample is thought to be due to the combination of several factors such as more oxygen vacancies, improved reducibility and enhanced surface area.

3.2.2 *Soot Oxidation*

The activity of CeO_2, CZ, CL, CZY, and CLY samples is also studied for soot oxidation and the corresponding profiles are shown in Fig. 9. For comparison, the oxidation of soot without catalyst is also included. In order to clearly compare the catalytic activity of the catalysts for soot oxidation, we have defined the temperature value T_{50} at which the 50 % of soot conversion was obtained and the results are illustrated in Table 3. Compared to that without any catalyst, the T_{50} for soot oxidation decreased with catalyst in the following order: CLY (732 K) > CL (742 K) ≈ CZY (743 K) > CZ (795 K) > CeO_2 (874 K) > no catalyst (922 K). This trend clearly indicates that the Y dopant significantly improved the soot oxidation activity of CZ and CL samples. Moreover, CLY exhibits higher activity than the CZY and it lowered the T_{50} remarkably by 190 K in comparison with that of soot alone. Noticeably, CZY, CL, CZ, and CeO_2 samples showed only 44.4, 44.4, 18.9, and 9.6 % conversion at T_{50} temperature of CLY (Table 3). This improved catalytic performance can be attributed to a higher surface area of the CLY sample. However, the T_{50} of CL is similar to that of CZY while it is lower than the CZ, although its surface area is much lower than the CZY and CZ samples. These results indicate that, besides surface area, there are some other factors affecting the catalytic activity for soot oxidation which are described in the following paragraph.

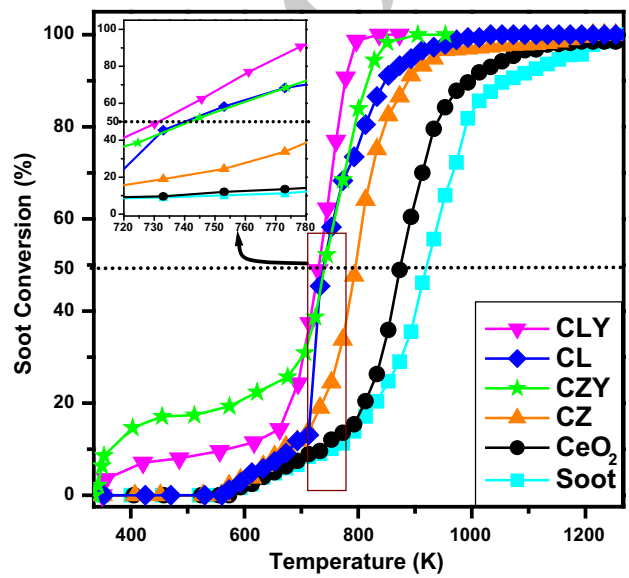

Fig. 9 Catalytic activity of pure CeO_2, undoped and Y-doped ceria–zirconia and ceria lanthana solid solutions for soot oxidation (*inset* expanded view of selected region)

It is known that the oxygen vacancies are the other important active sites for soot oxidation which are able to promote adsorption–activation of reactant molecule (O_2) [15]. The oxygen vacancy concentration follows the above observed activity order confirmed from Raman and XPS analyses. Therefore, similar to CO oxidation, oxygen vacancies are more favourable to improve the catalytic activity for soot oxidation. In particular, the higher catalytic performance of CLY among the samples is ascribed to the improved reducibility and more oxygen vacancies along with the increased surface area. Additionally, the difference in T_{50} is only 10 K between CLY and CL, whilst a remarkable difference (49 K) is observed between CZY and CZ. This result suggests that, similar to CO oxidation, Y dopant strongly effects on the soot oxidation activity of CZ compared to that of CL sample.

Journal : Large 10562 Dispatch : 3-3-2015 Pages : 11
Article No. : 1507 LE TYPESET
MS Code : CATLET-2014-1114 CP DISK

4 Conclusions

Y-doped CZ ($Ce_{0.8}Zr_{0.12}Y_{0.08}O_{2-\delta}$, CZY) and CL ($Ce_{0.8}La_{0.12}Y_{0.08}O_{2-\delta}$, CLY) ternary oxide solid solutions were synthesized using a coprecipitation method and characterized by XRD, ICP–OES, RS, UV–vis DRS, XPS, H_2-TPR, HRTEM, and BET SA techniques. XRD, Raman and UV–vis DRS characterizations suggested that the Y^{3+} ions were successfully doped into the CZ and CL samples by the formation of ternary oxide solid solutions. HRTEM analysis revealed the average particle sizes in a range of 4.8–8.6 nm in line with XRD results. RS, UV–vis DRS, and XPS studies disclosed that Y-doped CZ and CL samples had an increased quantity of oxygen vacancies compared to the undoped CZ and CL solid solutions, respectively. Moreover, H_2-TPR and BET results confirmed that Y doping improved the reducibility and surface area of CZ and CL samples, respectively. Based on these favorable properties, it is concluded that CO and soot oxidation performance was greatly improved upon Y-doping into the CZ and CL samples. Particularly, it was found that the CLY showed the best catalytic activity among the investigated samples, which contributed to the highest amount of oxygen vacancies, the highest reducibility as well as the enhanced surface area.

Acknowledgments We gratefully acknowledge Department of Science and Technology (DST), New Delhi for financial support of this work. D.D. thanks the Department of Education, Australian Government for providing Endeavour Research Fellowship.

References

1. Qadir K, Joo SH, Mun BS, Butcher DR, Renzas JR, Aksoy F, Liu Z, Somorjai GA, Park JY (2012) Nano Lett 12:5761–5768
2. Kurnatowska M, Mista W, Mazur P, Kepinski L (2014) Appl Catal B Environ 148–149:123–135
3. Ma S, Lu G, Shen Y, Guo Y, Wang Y, Guo Y (2011) Catal Sci Technol 1:669–674
4. Aneggi E, Wiater D, de Leitenburg C, Llorca J, Trovarelli A (2014) ACS Catal 4:172–181
5. Paier J, Penschke C, Sauer J (2013) Chem Rev 113:3949–3985
6. Chen W-T, Chen K-B, Wang M-F, Weng S-F, Lee C-S, Lin MC (2010) Chem Commun 46:3286–3288
7. Reddy BM, Bharali P, Saikia P, Khan A, Loridant S, Muhler M, Grünert W (2007) J Phys Chem C 111:1878–1881
8. Reddy BM, Katta L, Thrimurthulu G (2010) Chem Mater 22:467–475
9. Reddy BM, Thrimurthulu G, Katta L, Yamada Y, Park S-E (2009) J Phys Chem C 113:15882–15890
10. Reddy BM, Thrimurthulu G, Katta L (2011) Catal Lett 141:572–581
11. Cai W, Zhong Q, Zhang S, Zhang J (2013) RSC Adv 3:7009–7015
12. Atribak I, Bueno-López A, García-García A (2008) Catal Commun 9:250–255
13. Fornasiero P, Fonda E, Monte RD, Vlaic G, Kašpar J, Graziani M (1999) J Catal 187:177–185
14. Thammachart M, Meeyoo V, Risksomboon T, Osuwan S (2001) Catal Today 68:53–61
15. Aneggi E, de Leitenburg C, Trovarelli A (2012) Catal Today 181:108–115
16. Katta L, Sudarsanam P, Thrimurthulu G, Reddy BM (2010) Appl Catal B Environ 101:101–108
17. Cai S, Zhang D, Zhang L, Huang L, Li H, Gao R, Shiab L, Zhang J (2014) Catal Sci Technol 4:93–101
18. Dasari HP, Ahn K, Park S-Y, Ji H-I, Yoon KJ, Kim B-K, Je H-J, Lee H-W, Lee J-H (2013) Int J Hydrogen Energy 38:6097–6103
19. Prasad DH, Park SY, Ji H-I, Kim H-R, Son J-W, Kim B-K, Lee H-W, Lee J-H (2012) J Phys Chem C 116:3467–3476
20. Li G, Wang Q, Zhao B, Zhou R (2012) Fuel 92:360–368
21. Bharali P, Saikia P, Katta L, Reddy BM (2013) J Ind Eng Chem 19:327–336
22. Si R, Zhang Y-W, Wang L-M, Li S-J, Lin B-X, Chu W-S, Wu Z-Y, Yan C- H (2007) J Phys Chem C 111:787–794
23. Atribak I, Bueno-López A, García-García A (2009) J Mol Catal A 300:103–110
24. He H, Dai HX, Ng LH, Wong KW, Au CT (2002) J Catal 206:1–13
25. He H, Dai HX, Wong KW, Au CT (2003) Appl Catal A Gen 251:61–74
26. He H, Dai HX, Au CT (2004) Catal Today 90:245–254
27. Yao X, Tang C, Ji Z, Dai Y, Cao Y, Gao F, Dong L, Chen Y (2013) Catal Sci Technol 3:688–698
28. Harshini D, Lee DH, Jeong J, Kim Y, Nam SW, Ham HC, Han JH, Lim T-H, Yoon CW (2014) Appl Catal B Environ 148–149:415–423
29. Hernández-Giménez AM, dos Santos Xavier LP, Bueno-López A (2013) Appl Catal A Gen 462–463:100–106
30. Li L, Chen F, Lu J-Q, Luo M-F (2011) J Phys Chem A 115:7972–7977
31. Paunović N, Dohčević-Mitrović Z, Scurtu R, Aškrabić S, Prekajski M, Matović B, Popović ZV (2012) Nanoscale 4:5469–5476
32. Guo M, Lu J, Wu Y, Wang Y, Luo M (2011) Langmuir 27:3872–3877
33. Romeo M, Bak K, Fallah JE, Normand FL, Hilaire L (1993) Surf Interface Anal 20:508–512
34. Reddy BM, Katta L, Thrimurthulu G (2001) Catal Today 175:585–592
35. Qu Z, Yu F, Zhang X, Wang Y, Gao J (2013) Chem Eng J 229:522–532
36. Yang D, Wang L, Sun Y, Zhou K (2010) J Phys Chem C 114:8926–8932
37. Wagner CD, Riggs WM, Davis LE, Moulder JF (1978) In: Muilenberg GE (ed) Handbook of X-ray photoelectron spectroscopy. Perkin-Elmer Corporation, Eden Prairie
38. Zhang Y, Zhang L, Deng J, Dai H, He H (2009) Inorg Chem 48:2181–2192
39. Durgasri DN, Vinodkumar T, Sudarsanam P, Reddy BM (2014) Catal Lett 144:971–979

Journal : Large 10562 | Dispatch : 3-3-2015 | Pages : 11
Article No. : 1507 | LE | TYPESET
MS Code : CATLET-2014-1114 | CP | DISK